Evaluation of Long-term Settlement of a Large Building on a Piled Raft in Soft Ground Using SAR Remote Sensing
SARリモートセンシングによる軟弱地盤上のパイルド・ラフト基礎に支持される大規模建物の長期沈下評価

Tomohiro Tanikawa 谷川 友浩*1 Junji Hamada 濱田 純次*2
Kiyoshi Yamashita 山下 清*3

Summary

This paper undertakes a comparative analysis of the long-term settlements of a low-rise parking structure supported by a piled raft foundation in reclaimed ground. The conventional leveling measurements are compared with those obtained by multi-temporal InSAR analysis. The vertical displacements obtained from the InSAR analysis are found to be generally in good agreement with those from the leveling measurements. The study demonstrates the effectiveness of SAR analysis for monitoring vertical displacements of buildings on soft ground.

Keywords: consolidation settlement, remote sensing, InSAR, piled raft foundation

梗 概

軟弱地盤に建つパイルド・ラフト基礎で支持された低層の立体駐車場の長期的な沈下について，従来の水準測量で得られた沈下測定結果と時系列干渉SAR解析（InSAR解析）で得られた結果を比較した。InSAR解析から得られた鉛直変位は，水準測量から得られたものと良好な一致を示していることがわかり，軟弱地盤上の建物の鉛直変位モニタリングにおけるSAR解析の有用性を実証している。

キーワード：圧密沈下，リモートセンシング，時系列干渉SAR解析，パイルド・ラフト基礎

1 INTRODUCTION

The growing consideration of environmental impacts has led to the widespread adoption of piled raft foundations, wherein the contribution of a raft to the total resistance of a piled foundation is incorporated in the design process. Given that piled rafts are based on a displacement-based design approach, it is crucial to assess their deformation performance. Consequently, there is an urgent need to develop an accurate and highly efficient method for evaluating the performance of the foundations, in addition to conventional geodetic techniques such as leveling measurements.

Interferometric Synthetic Aperture Radar (InSAR) is an Earth observation technique based on radar satellite imagery that can measure surface deformation with millimetric level precision (Gabriel et al., 1989; Rosen et al., 2000; Sadeghi et al., 2021). Synthetic Aperture Radar (SAR) observation data are obtained by emitting microwaves from a satellite SAR to the Earth's surface and recording the reflected signals. This technique has the advantage of allowing observation without the need to install equipment on the Earth's surface, regardless of weather conditions, both during the day and at night. Persistent Scatterer Interferometry (PSI), first proposed by Ferretti et al. (2001), is a powerful remote sensing technique that exploits multi-temporal SAR images acquired over the same area to measure and monitor the displacement of the Earth's surface over time (Crosetto et al., 2016). The development of multi-temporal InSAR techniques, such as PSI, has enabled the acquisition of highly accurate deformation time series. Multi-temporal InSAR techniques have been extensively utilized to monitor urban areas affected by subsidence at regional and local scales in the context of very slow displacements (e.g., Cigna et al., 2012, 2014; Raspini et al., 2012; Rosi et al., 2014). These techniques have also been employed in analyses at the building and infrastructure scale (Solari et al., 2016; Ciampalini et al., 2019; Hoppe et al., 2019; Wu et al., 2020). In Japan, the utilization of

＊1 Senior Chief Researcher, Research & Development Institute. 技術研究所 主席研究員
＊2 Senior Chief Researcher, Research & Development Institute, Dr. Eng. 技術研究所 主席研究員 博士（工学）
＊3 Formerly, Research & Development Institute, Takenaka Corporation, Dr. Eng. 元(株)竹中工務店技術研究所 博士（工学）

multi-temporal InSAR techniques has recently been considered as a means of enhancing the efficacy of the maintenance and management of social infrastructure, including rockfill dams, road soil structures, and river levees (Sato et al., 2017; Koseki et al., 2018; Kubota et al., 2024). Nevertheless, there are few case studies that compare InSAR results with overall and differential settlement from conventional leveling in detail for a specific building.

This paper presents a case study of a large low-rise building supported by a friction piled raft foundation in soft ground. Long-term settlement monitoring of the building was conducted using conventional geodetic techniques from the beginning of construction in 2006 for more than fifteen years. The objective of this study is to evaluate the long-term deformation of the large building using satellite SAR remote sensing. To this end, the deformation time series of the building were estimated from multi-temporal InSAR analysis using medium-resolution images of the site obtained by the Sentinel-1 constellation over the period 2014 – 2021. The estimated vertical displacement time series were then compared with the leveling measurements in order to validate the InSAR results. A portion of this study was recently published by Tanikawa et al. (2025).

2 BUILDING UNDER STUDY

2.1 Structure and soil conditions

The building under study is a low-rise, multi-story parking structure situated in a reclaimed area on the Tokyo Bay coast (Yamashita et al., 2019). Fig. 1 presents a longitudinal view of the building with soil profiles and Fig. 2 shows a foundation plan view. The building is constructed of steel-reinforced concrete columns and steel beams, with a plan area of 213 m by 71 m. The mean load per unit area over the raft was 45 kPa. The soil profile consists of a layer of filled sand and alluvial loose sand extending to a depth of 10 – 15 m. Below this, there is a layer of soft alluvial clay deposits, which are normally consolidated (or still under-consolidated). The ground water table is approximately 1.5 m below the surface. The thickness of the alluvial clay deposits exhibits a significant change in the central region of the site, attributed to the presence of a buried valley.

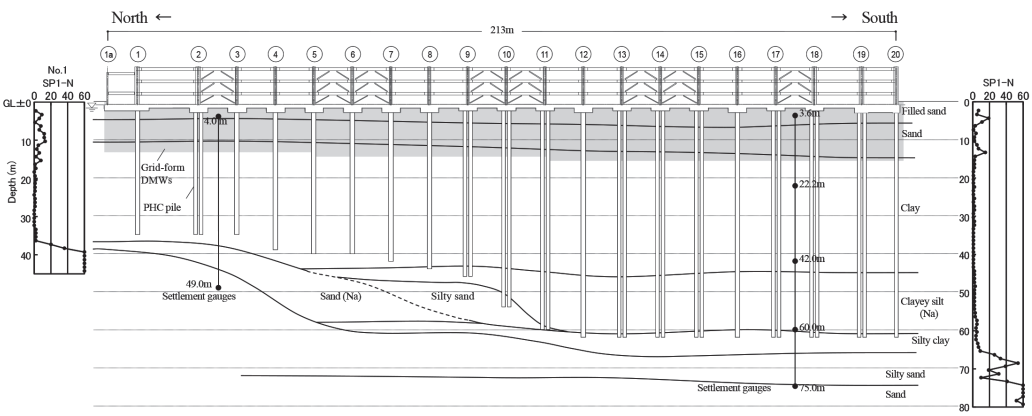

Fig. 1 Building and foundation with monitoring equipment locations: longitudinal view with soil profiles

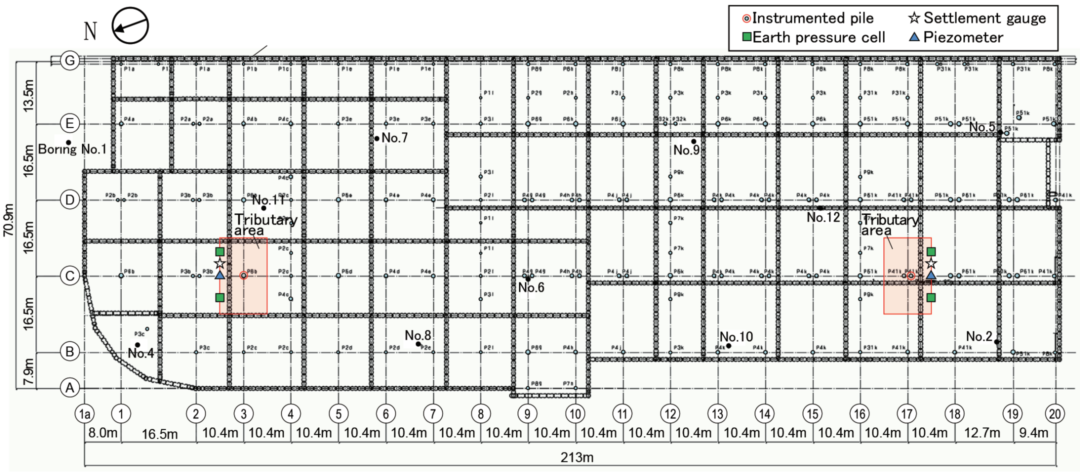

Fig. 2 Building and foundation with monitoring equipment locations: foundation plan view

2.2 Foundation

Given that the superstructure load per unit area is relatively low and that the structure is intended for a parking lot, which allows for some total and differential settlement, the foundation was designed based on a displacement-based approach and a friction piled raft foundation was selected. In the friction piled raft, 152 PHC piles with diameters of 0.5 – 1.0 m were used. The depth of the pile toe is 35 – 42 m from the ground surface in the northern part and 62 m in the southern part, while the depth of the pile toe varies from 44 to 60 m in the central part. Moreover, a cement deep mixing wall (DMW) grid was employed as a countermeasure against the liquefaction of the filled sand and alluvial sand underlying the raft, as illustrated in Figs. 1 and 2.

2.3 Instrumentation

A comprehensive field monitoring program was initiated at the beginning of construction in 2006 and continued for more than fifteen years after the completion of the building. The program included the monitoring of foundation settlement and load sharing between the piles and the raft. The locations of the monitoring devices are illustrated in Figs. 1 and 2. Vertical ground displacements were measured beneath the raft, in the vicinity of column 3C and at four depths in the vicinity of column 17C, using differential settlement gauges. Leveling measurements were conducted at the selected columns on the first floor (see Fig. 6). A benchmark for the leveling measurements was established at column 3C, where it was assumed that the settlement would be equal to the settlement of the ground beneath the raft at a depth of 4.0 m from the ground surface, as obtained by the measurement of differential settlement gauges. The measurement process is still ongoing, and the degree of subsidence of the building and the ground is consistent, with no perceptible steps observed at the entrances. Further details regarding the field monitoring can be found in Yamashita et al. (2019).

2.4 Results of settlement monitoring

Fig. 3 shows the development of vertical ground displacement beneath the raft, as measured by differential settlement gauges. The vertical ground displacements beneath the raft, at a depth of 4.0 m in the vicinity of 3C and at a depth of 3.6 m in the vicinity of 17C, are shown in Fig. 3a. The ground displacements in the vicinity of 17C were found to be significantly greater than those near 3C, in accordance with the thickness of the alluvial clayey layers. A sudden increase in ground displacement was observed in the vicinity of 3C at the time of the 2011 Tohoku earthquake (*M*w = 9.0), while no significant increase in ground displacement was recorded in the vicinity of 17C. This can be attributed to the inelastic settlement of the relatively short friction piles used in the northern part of the piled raft, which were subjected to the strong seismic axial loading. It should be noted that since the measurement of differential settlement gauges in the vicinity of 3C ceased in 2017 due to disconnection, the "log *t*" approximation based on the data after the seismic event has been employed to extrapolate the settlement at the benchmark, as illustrated by the dotted line. Fig. 3b shows the vertical ground displacement in each soil layer beneath the raft in the vicinity of 17C in the southern part. The measured displacements of the layers deeper than 42.0 m depth were considerably large, indicating that the clayey silt and silty clay layers between depths of 45 and 65 m were undergoing consolidation due to the combined effects of the building load and overburden pressure of the reclaimed ground. On the other hand, the measured displacements of the layers shallower than 42.0 m were very small, indicating that the consolidation settlement of the clay layer between depths of 15 and 45 m has been nearly complete.

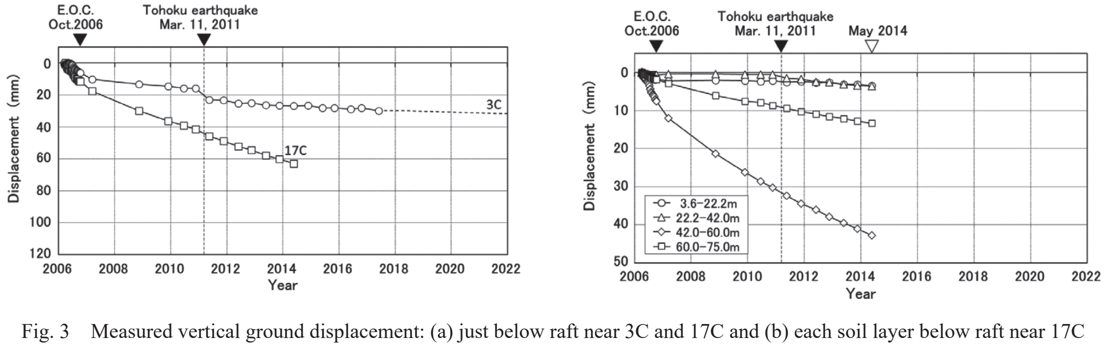

Fig. 3 Measured vertical ground displacement: (a) just below raft near 3C and 17C and (b) each soil layer below raft near 17C

Fig. 4 presents the settlement profiles on the first floor of the building in the longitudinal and transverse directions at the time of completion and subsequently. The settlement exhibited considerable variation across the columns, with values ranging from 22 mm at 1C to 121 mm at 17E on November 29, 2021. The greatest degree of settlement was observed on the southeast side, indicating that the building as a whole tilted to the south and east. The angular rotation along Street 17 between 17B and 17E in the transverse direction was 1/880, while the angular rotation along Street E between 11E and 17E in the longitudinal direction was 1/1330.

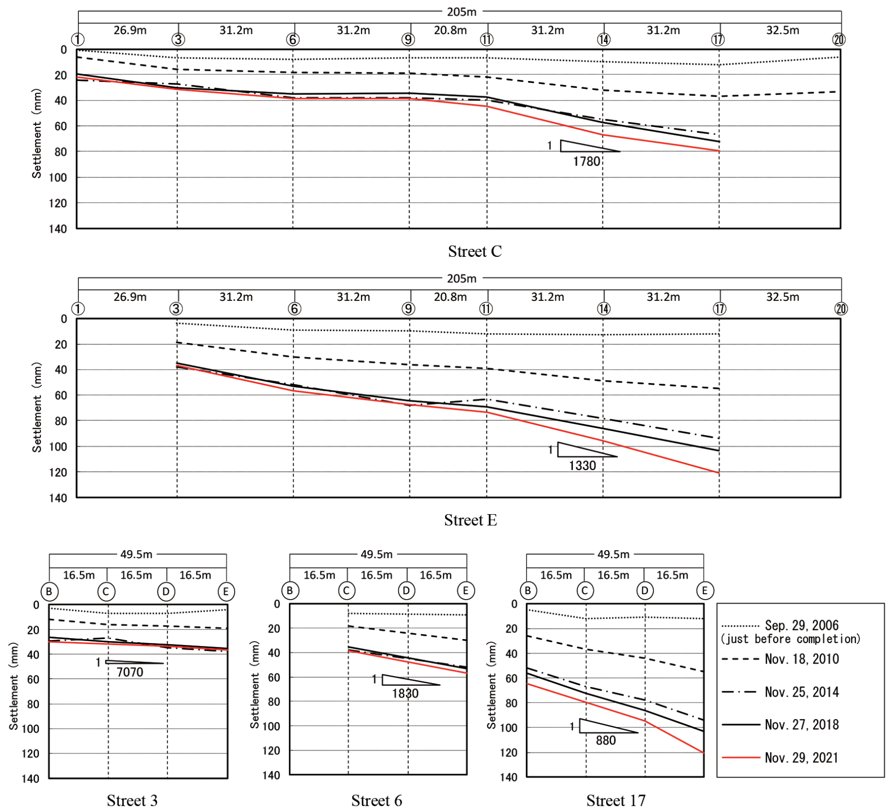

Fig. 4 Settlement profiles on the 1st floor of the building from leveling measurements

3 INSAR METHODOLOGY

3.1 SAR dataset

This study employed medium-resolution (C-band) SAR images obtained by the Sentinel-1 constellation, which consists of two satellites from the European Union and the European Space Agency's Copernicus Program (Sadeghi et al., 2021). Table 1 provides an overview of the technical specifications of the Sentinel-1. The SAR images of the site were acquired using both ascending (flying south to north, eastward-looking) and descending (flying north to south, westward-looking) geometries (see Fig. 6). A total of 169 images of the ascending geometry were acquired between April 30, 2015, and October 13, 2021, while 180 images of the descending geometry were acquired between November 25, 2014, and October 7, 2021. The acquired SAR images were processed by TRE ALTAMIRA using the SqueeSAR analysis (Ferretti et al., 2011). The SqueeSAR analysis enables the generation of a time series of the line-of-sight (LOS) displacement between a satellite and a measurement point on the Earth's surface (denoted MP) based on the phase difference information of the observation data. This is referred to as one-dimensional (1-D) analysis.

Table 1 Technical specifications of Sentinel-1 constellation

Band	Wavelength	Number of satellites	Revisiting time (one satellite)	Altitude	Beam mode	Swath width	Resolution
C	5.93 cm	2	12 days	693 km	Interferometric Wide Swath	250 km	5 m × 20 m

3.2 Estimation of vertical and horizontal deformation

The LOS displacement (D_{LOS}) is the projection of the 3-D real movement along the LOS and is given by Eq. (1) (Fuhrmann and Garthwaite, 2019).

$$D_{LOS} = D_v \cos\theta - D_E \sin\theta \cos\alpha + D_N \sin\theta \sin\alpha \quad (1)$$

where D_V, D_E and D_N are the vertical, eastward and northward components, respectively, of the real displacement vector of the radar target; θ is the incidence angle; and α is the azimuth angles of the satellite heading (angle between the satellite heading and true North). Since the satellite orbit is typically close to the north-south direction and microwaves are emitted in a direction perpendicular to the satellite orbit, displacement in the north-south direction is nearly undetectable from the satellite LOS direction. Therefore, by assuming $D_N = 0$ in Eq. (1), a system of Eqs. (2) and (3) is obtained for the ascending and descending geometries, respectively (Raspini et al., 2012; Cigna et al., 2019).

$$D_A = D_V \cos\theta_A - D_E \sin\theta_A \cos\alpha_A \quad (2)$$

$$D_D = D_V \cos\theta_D - D_E \sin\theta_D \cos\alpha_D \quad (3)$$

where D_A and D_D are the LOS displacements; θ_A and θ_D are the incidence angles; α_A and α_D are the azimuth angles of the satellite heading. The subscripts A and D indicate ascending and descending geometries, respectively. In the present case, the incidence angles θ_A and θ_D were 41.7° and 38.5°, respectively, and the azimuth angles α_A and α_D were 350.8° and 190.2°, respectively (see Fig. 6). As illustrated in Fig. 5, the satellite LOS displacement for the ascending and descending geometries is related to the real displacement (D_{real}) in a two-dimensional (2-D) analysis.

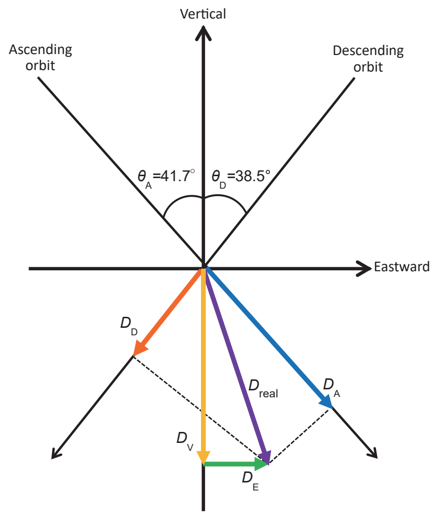

Fig. 5 Relationship between LOS displacement for the ascending and descending geometries and real displacement (2-D analysis)

When information from both ascending and descending datasets is available for the same area in the same time period, the components of the real displacement vector along the vertical and east-west directions are obtained by solving the system of Eqs. (2) and (3). The solution of this system requires that a single MP is recognized as a valid target by the satellite in both ascending and descending orbits. However, this condition rarely occurs, necessitating the creation of artificial MPs. This operation can be performed by dividing the space into a sampling grid of square cells (as shown in Fig. 6) and calculating the mean deformation in the cell for each of the two orbits (Rosi et al., 2014; Cigna et al., 2019). If the observation dates of both orbits do not coincide, the displacement is obtained by interpolating the displacement between the previous and subsequent observation dates. The vertical and east-west components of the real displacement vector are denoted as D_V and D_E, respectively.

In the context of static loading conditions, it can be assumed that the predominant component of the real motion of ground and structure is in the vertical direction. In such cases, the horizontal displacements can be neglected, resulting in $D_E = D_N = 0$ in Eq. (1). Consequently, the vertical components of the real displacement vector can be estimated from the following Eqs. (4) and (5), provided that the LOS displacements are available for either ascending or descending geometry (Cigna et al., 2014).

$$D_{VA} = D_A / \cos\theta_A \quad (4)$$

$$D_{VD} = D_D / \cos\theta_D \quad (5)$$

where D_{VA} and D_{VD} are the vertical components estimated from the ascending and descending LOS displacements, respectively. The vertical components estimated from Eqs. (4) and (5) are hereafter referred to as 1-D-derived vertical displacements.

4 INSAR RESULTS

Fig. 6 illustrates the distribution of the identified MPs within the building envelope, as determined by the SqueeSAR analysis. The ascending and descending geometries are presented separately. The latitude and longitude coordinates of the building plan were determined using GSI Maps (provided by the Geospatial Information Authority of Japan), with the southeast angle of the building adjusted to match that on the GSI Maps. Within the building envelope, 33 and 61 MPs were identified for the ascending and descending geometries, respectively. The direction of satellite orbit travel and the direction of microwave irradiation are indicated by the blue arrows. Fig. 6 also shows the locations of the leveling measurement columns and a sampling grid consisting of 20x20 m square cells, each identified by a cell number. The grid is employed to estimate the vertical and eastward displacements (Rosi et al., 2014), as well as to identify the MPs corresponding to the leveling points.

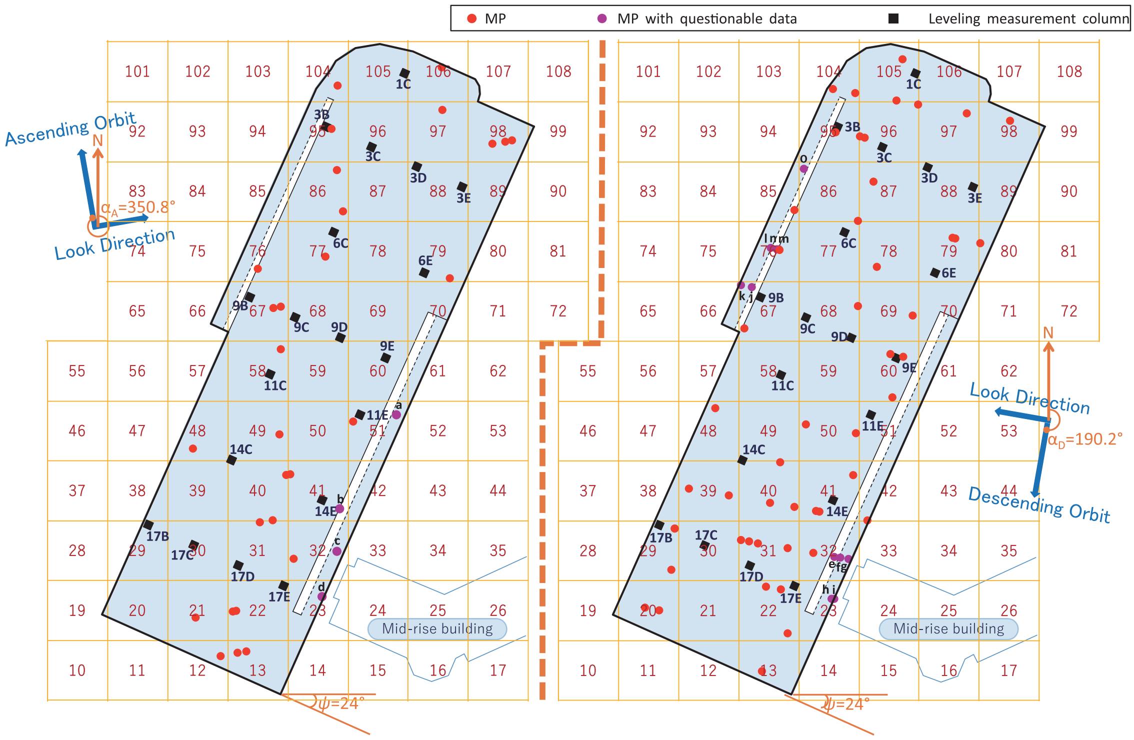

(a) Ascending geometry (b) Descending geometry

Fig. 6 Distribution of MPs inside the building with the locations of leveling measurement columns and a sampling grid

4.1 LOS displacements

Figs. 7 and 8 show the estimated time series of the LOS displacement at the MPs in each cell containing the MPs, for ascending and descending geometries, respectively. The symbol # represents the number of the cell shown in Fig. 6. The LOS displacement is the increase in value relative to the value at the time of the initial acquisition. The direction of the MP's movement with respect to the satellite can be determined by the sign of the displacement. A positive displacement indicates that the MP is moving towards the satellite, while a negative displacement indicates that it is moving away from the satellite. Although there is some transient data scatter, the LOS displacement time series exhibited a nearly linear increase over time for both ascending and descending geometries. The periodic deformation pattern is observed in the displacement time series, particularly evident in cells such as #106 and #97 in Fig. 7 and #69 and #60 in Fig. 8. This is likely the result of thermal dilation of the portion of the roof due to seasonal temperature fluctuations observed in the scene (Crosetto et al., 2008).

When multiple MPs were present in the same cell, the displacement time series in the cell appeared to be generally consistent. However, the displacements at MPs indicated by a, b, c, and d (where the MPs a, c, and d are located on the ramp to the rooftop), shown as purple dots in Fig. 6a, were significantly smaller than those at MPs in the same cell or nearby cells, as shown by the red line in Fig. 7. Possible explanations for the observed issues are as follows: In the ascending geometry, the LOS to the MPs a and b may be obstructed by the roof of the building. For MPs c and d in the vicinity of the mid-rise building, there appears to be an effect of microwaves reflected from the adjacent building on the backscattered signals from the MPs. In the descending geometry (Fig. 6b), the LOS to the MPs e, f, g, h, and i in the vicinity of the mid-rise building may be affected by shadowing from the building. In addition, the LOS to the MPs j, k, l, m, n, and o located on the ramp on the northwest side may also be affected by shadowing from the roof of the building. The time series of LOS displacements at the MPs e, f, g, h, i, j, k, l, m, n, and o, as illustrated by the red line in Fig. 8, indicate that the LOS displacements at most of these MPs are significantly small. Therefore, it is necessary to pay close attention to the positions of the MP identified in the analysis and the surrounding conditions.

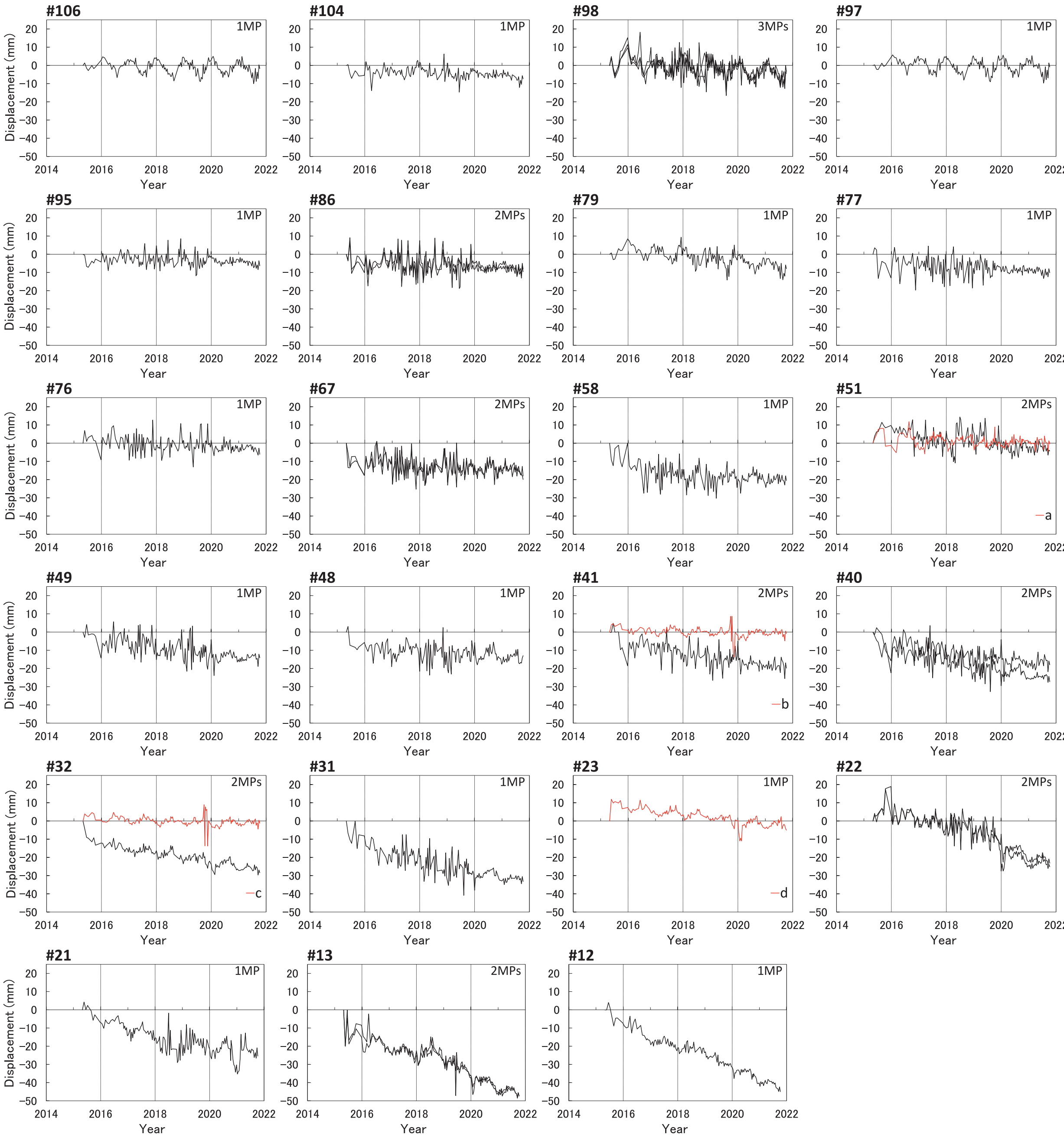

Fig. 7 LOS displacement time series at MPs inside the building envelope line for ascending geometry

Fig. 9 presents the time series of mean LOS displacements in the cell containing the leveling points for both geometries. The mean LOS displacement is the average of the LOS displacements in the case of multiple MPs in the same cell. In calculating the mean LOS displacements, we excluded the LOS displacements at MPs a and b, in cells #51 and #41, respectively, for the ascending geometry and MPs j and k in cell #67 for the descending geometry. This was done in order to address the possibility of questionable measurements, as previously mentioned.

The specific displacement time series in some cells indicate a clear tendency for shifts in either the positive or negative direction. The underlying causes of these shifts remain uncertain; however, in order to mitigate the impact of discrepancies in comparisons with independent estimates, such as leveling measurements, a linear regression was used to correct shifts in the displacement time series. The corrected displacement history is represented by the blue dots, with the initial value of the linear regression line (indicated by the red dashed line) being zero. Furthermore, it is observed that while there is some transient scatter in the mean LOS displacement histories, the magnitude of the scatter appears to be greater for InSAR results obtained from a single MP or two MPs within the cell (denoted as 1 MP or 2 MPs, respectively), but smaller for those obtained from three or four MPs within the cell.

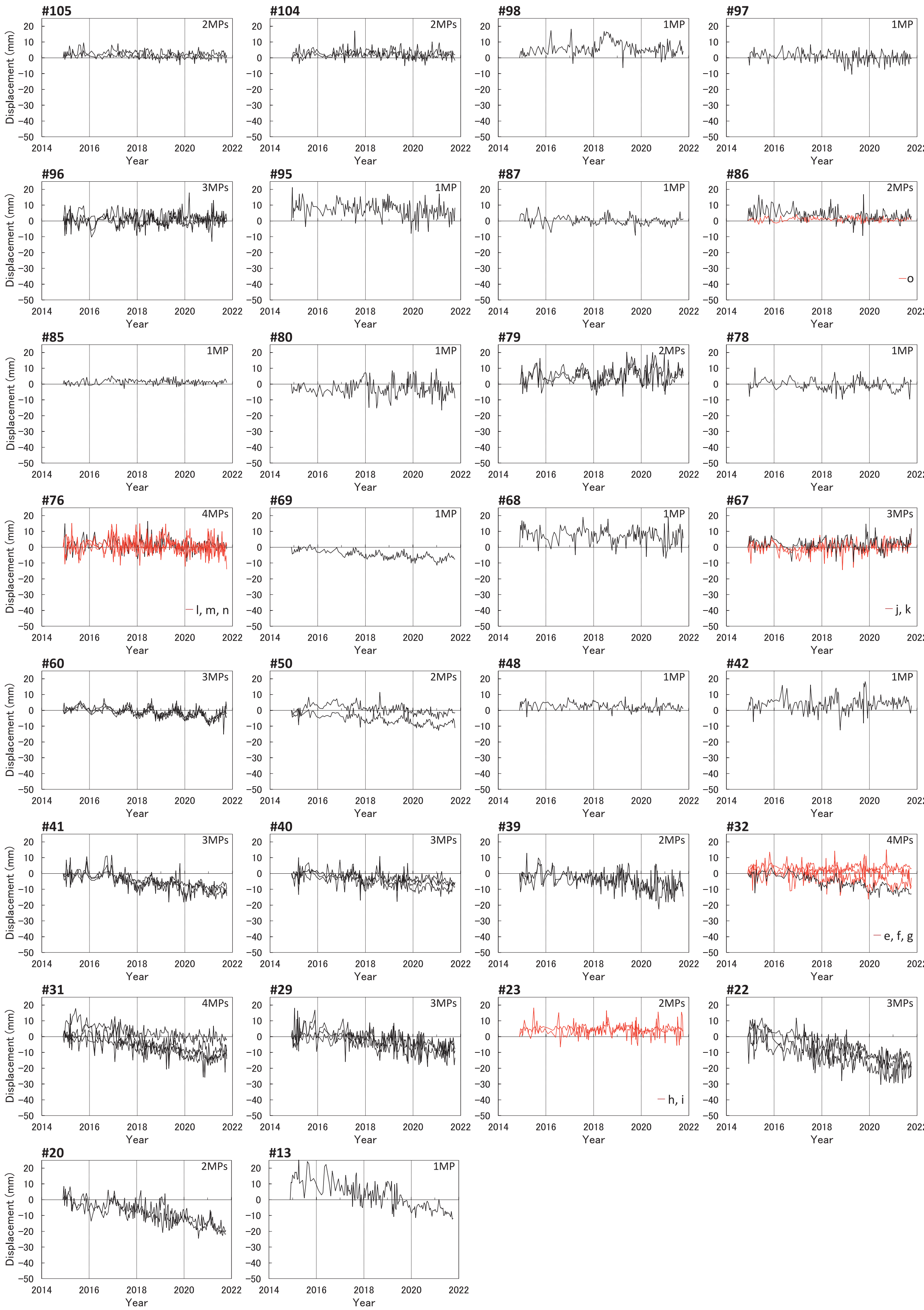

Fig. 8 LOS displacement time series at MPs inside the building envelope line for descending geometry

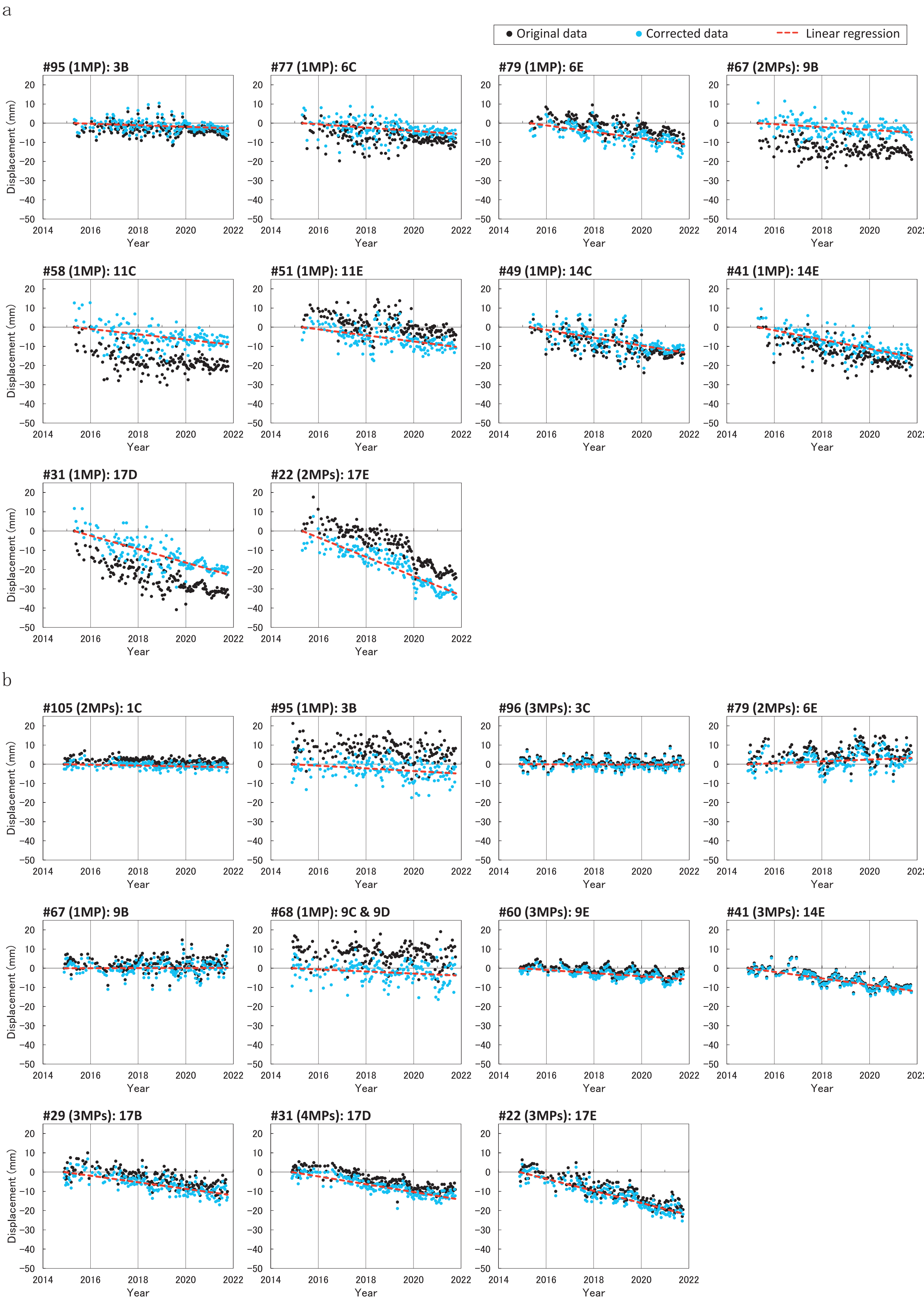

Fig. 9 Time series of mean LOS displacements in the cell containing leveling points: (a) ascending and (b) descending geometries

4.2 2-D displacements

In order to evaluate the vertical and eastward displacements, it is necessary to obtain the LOS displacements from the ascending and descending geometries in the same cell, as discussed in **3.2.** From the SqueeSAR analysis, the 2-D displacements were obtained for the six cells (#95, #79, #67, #41, #31, and #22) containing the leveling points 3B, 6E, 9B, 14E, 17D, and 17E, respectively. It should be noted, however, that the displacements at MP b in #41 and MPs j and k in #67 have been identified as questionable data, as discussed in **4.1.** Consequently, the 2-D displacements of #41 and #67 have been excluded from the discussion in this paper.

Fig. 10 presents the 2-D time series of the vertical displacement in the four cells #95, #79, #31, and #22, containing leveling points 3B, 6E, 17D, and 17E, respectively. The initial point of the 2-D displacements is April 30, 2015, which is the same as the ascending data. As with the mean LOS displacement time series in Fig. 9, a linear regression was employed to correct for the shift in the original displacement history.

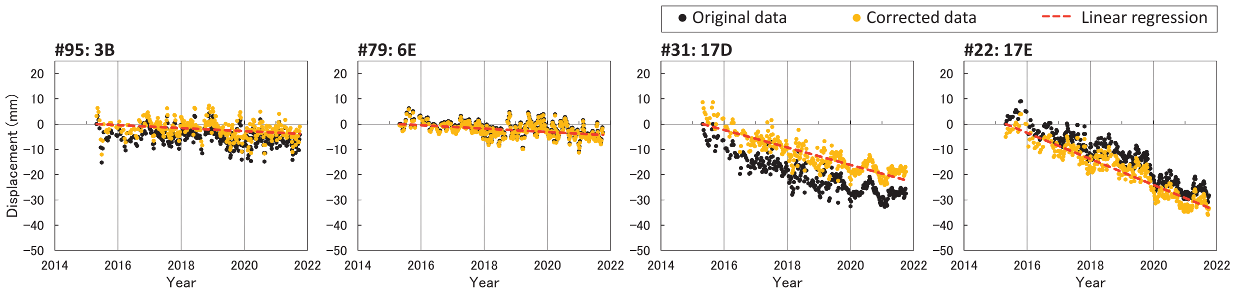

Fig. 10 Vertical displacement (D_V) time series in the four cells containing levelling points 3B, 6E, 17D, and 17E

5 VALIDATION OF INSAR RESULTS

The validation of the InSAR results for vertical displacements was based on a comparison of the displacement time series with the leveling measurements presented in **Section 2**.

First, the 1-D-derived vertical displacements are compared to the leveling measurements, as illustrated in Fig. 11 for the ascending and descending geometries, respectively. Note that in Fig. 11b, the leveling measurements at points 9C and 9D are compared to the same 1-D-derived vertical displacements in cell #68. In order to mitigate the impact of scatter in the leveling measurements in the comparison, a hyperbolic approximation of the leveling measurements was introduced. The shape of the time-series curve of the subsidence from the leveling measurements after the 2011 Tohoku earthquake shows a slightly larger downward convex curvature compared to before the earthquake. Therefore, to appropriately evaluate the temporal variations in subsidence subsequent to the substantial seismic event, the initial point of the hyperbolic curve was set to November 18, 2010, preceding the event. The corrected 1-D-derived vertical displacements shown in Fig. 9 were employed for the comparison. The initial value of the vertical displacement was established based on the value of the hyperbolic curve at the time of the initial data acquisition (on April 30, 2015 for the ascending geometry and November 25, 2014 for the descending geometry). From November 25, 2014 to October 13, 2021, which corresponds to the SAR data acquisition period, the increment of the leveling measurements ranged from 1 to 27 mm, depending on the location of the leveling point. The 1-D-derived vertical displacements, with some allowance for transient data scatter, are somewhat larger in cells #31 and #22 (containing 17D and 17E, respectively) for the ascending geometry and smaller in cell #79 (containing 6E) for the descending geometry in comparison to the leveling measurements. Nevertheless, the overall agreement between the two sets of measurements is generally satisfactory. A subsequent comparison is presented between the vertical displacement time series in the four cells #95, #79, #31, and #22 and the leveling measurements at the corresponding points 3B, 6E, 17D, and 17E, as illustrated in Fig. 12. The vertical displacements were found to be in good agreement with the leveling measurements.

The following paragraphs will examine the discrepancies between the 1-D-derived vertical displacements and the leveling measurements in specific cells previously mentioned. As indicated in **2.4**, the building exhibited a slight tilt to the south and east after its completion. As illustrated in Fig. 4, on November 29, 2021 (immediately following the final SAR acquisition on October 13, 2021), the inclination angle along Street 17 (between leveling points 17B and 17E) in the transverse direction was

1/880. The inclination angle along Street 6 (between 6C and 6E) was found to be 1/1830, while the angle along Street 3 (between 3B and 3E) was 1/7070.

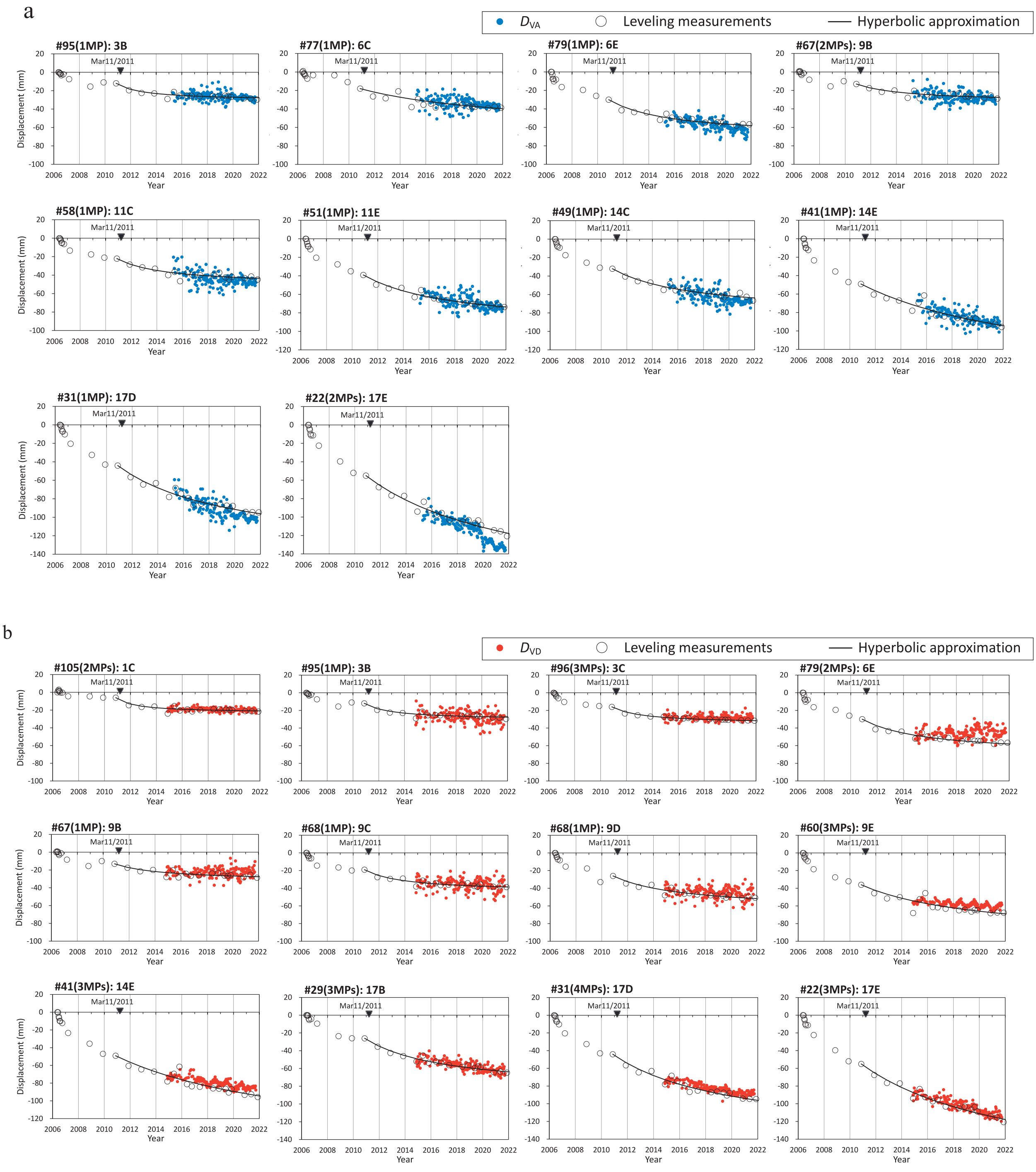

Fig. 11 Comparison of 1-D-derived vertical displacement with leveling measurements: (a) ascending and (b) descending geometries

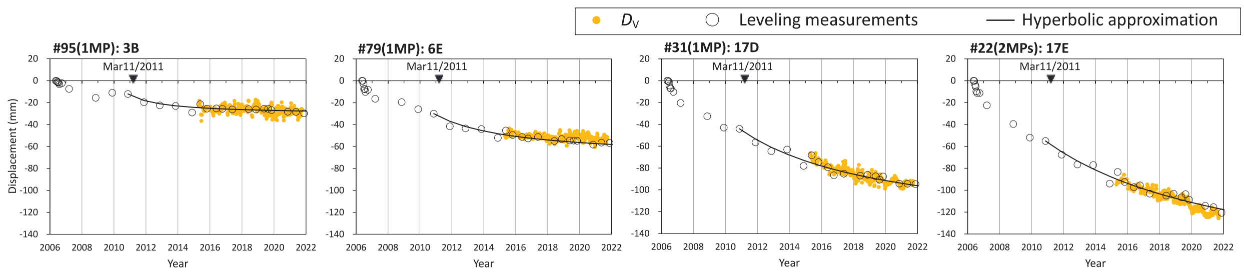

Fig. 12 Comparison of time series of vertical displacement (D_V) with leveling measurements

As shown in Fig. 13, a detailed comparison is provided of the vertical displacements with the 1-D-derived vertical displacements, along with the hyperbolic approximation of the leveling measurements. The initial value of the hyperbolic curve was set to zero on November 25, 2014, the date of the first data acquisition for the ascending geometry. The 1-D-derived vertical displacements from the ascending geometry (D_{VA}) are considerably greater than those from the descending geometry (D_{VD}) in cells #31 and #22 (containing 17D and 17E, respectively). In contrast, the values of D_{VA} and D_{VD} are comparable in cell #95 (containing 3B). As illustrated in Fig. 5, this indicates that the eastward displacements (approximately transverse direction of the building) near columns 17D and 17E on the rooftop are greater than the displacements near column 3B. In summary, the observed discrepancies between the 1-D-derived vertical displacements and the leveling measurements in cells #31 and #22 (which contain 17D and 17E) may be attributed to the effect of the inclination in the southern part of the building. This finding aligns with the observations made in previous studies, which noted that the assumption of zero horizontal displacement may introduce bias in the interpretation of results in zones exhibiting significant horizontal displacement (e.g., Cigna et al., 2019). However, in cell #79 (at 6E), the values of D_{VA} appear to be significantly different from those of D_{VD}, despite the inclination angle along Street 6 being relatively modest (1/1830). The reason for this discrepancy is currently unclear. As illustrated in Fig. 13, the vertical displacements appear to be intermediate between the 1-D-derived vertical displacements from the two geometries in cells #79, #31, and #22. Additionally, the vertical displacements are comparable to the 1-D-derived vertical displacements from the two geometries in cell #95. Consequently, the vertical displacement time series were in good agreement with the leveling measurements, as would be anticipated, irrespective of the building's appreciable or negligible tilt. However, the number of cells from which 2-D displacements could be obtained was limited.

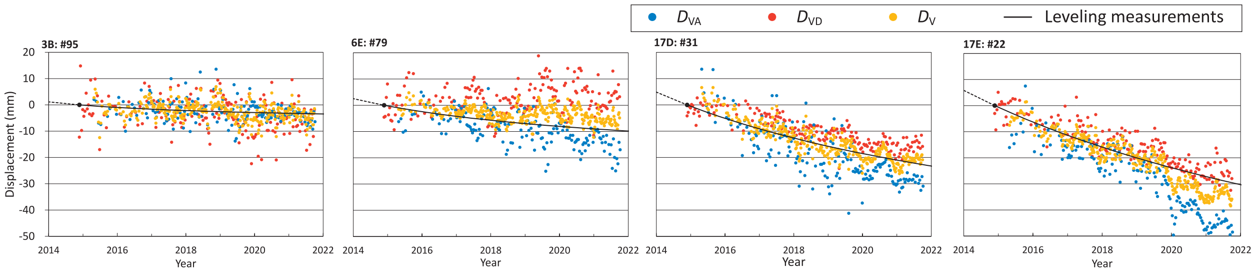

Fig. 13 Comparison of vertical displacements (D_V) with 1-D-derived vertical displacements (D_{VA}, D_{VD}) and leveling measurements

6 CONCLUSIONS

Through a comparison of the InSAR results and leveling measurements, the following conclusions were drawn:

1) A total of 33 and 61 MPs within the building envelope were identified from the InSAR analysis for the ascending and descending geometries, respectively. While there is some transient data scatter, at almost all MPs, the estimated LOS displacement time series exhibited a nearly linear increase over time.
2) When the satellite LOS displacements were available for either ascending or descending geometry, the 1-D-derived vertical displacement time series, derived from the assumption of zero horizontal displacement of the building, were found to be generally consistent with the leveling measurements. However, discrepancies were observed in a few cells between the two data sets, which may be attributed to the tilt of the building.
3) While the number of cells from which 2-D displacements could be obtained was limited, the vertical displacement time series were in good agreement with the leveling measurements, regardless of whether the tilt of the building was appreciable or negligible.
4) The utilization of C-band SAR images acquired by the Sentinel-1 constellation has the potential to serve as an effective tool for the assessment of long-term settlement of a substantial structure on soft deposits.

REFERENCES

Ciampalini, A., Solari, L., Giannecchini, R., Galanti, Y., Moretti, S., 2019. Evaluation of subsidence induced by long-lasting buildings load using InSAR technique and geotechnical data: The case study of a Freight Terminal (Tuscany, Italy). Int J

Appl Earth Obs Geoinformation. 82, 101925.

Cigna, F., Osmanoğlu, B., Cabral-Cano, E., Dixon, T. H., Ávila-Olivera, J. A., Garduño-Monroy, V. H., DeMets, C., Wdowinski, S., 2012. Monitoring land subsidence and its induced geological hazard with Synthetic Aperture Radar Interferometry: A case study in Morelia, Mexico. Remote Sensing of Environment. 117, 146–161.

Cigna, F., Lasaponara, R., Masini, N., Milillo, P., Tapete, D., 2014. Persistent scatterer interferometry processing of COSMO-SkyMed StripMap HIMAGE time series to depict deformation of the historic centre of Rome, Italy. Remote Sens. 6, 12593–12618.

Cigna, F., Tapete, D., Garduño-Monroy, V. H, Muñiz-Jauregui, J. A., García-Hernández, O. H., Jiménez-Haro, A., 2019. Wide-area InSAR survey of surface deformation in urban areas and geothermal fields in the Eastern Trans-Mexican volcanic belt, Mexico. Remote Sens. 11, 2341.

Crosetto, M., Biescas, E., Duro, J., Closa, J., Arnaud, A., 2008. Generation of advanced ERS and Envisat interferometric SAR products using the stable point network technique. Photogram. Eng. Remote Sens. 74 (4), 443–450.

Crosetto, M., Monserrat, O., Cuevas-González, M., Devanthéry, N., Crippa, B., 2016. Persistent scatterer interferometry: A review. ISPRS Journal of Photogrammetry and Remote Sensing. 115, 78–89.

Ferretti, A., Prati, C., Rocca, F., 2001. Permanent scatterers in SAR interferometry. IEEE Trans. Trans. Geosci. Remote. Sens. 39 (1), 8–20.

Ferretti, A., Fumagalli, A., Novali, F., Prati, C., Rocca, F., Rucci, A., 2011. A new algorithm for processing interferometric data-stacks: SqueeSAR. IEEE Trans. Geosci. Remote. Sens. 49 (9), 3460–3470.

Fuhrmann, T., Garthwaite, M. C., 2019. Resolving three-dimensional surface motion with InSAR: Constraints from multi-geometry data fusion. Remote Sens. 11, 241.

Gabriel, A. K., Goldstein, R. M., Zebker, H. A., 1989. Mapping small elevation changes over large areas: differential radar interferometry. J. Geophys. Res. 94 (B7), 9183–9191.

Hoppe, E. J., Novali, F., Alessio Rucci, A., Fumagalli, A., Conte, S. D., Falorni, G., Toro, N., 2019. Deformation monitoring of posttensioned bridges using high-resolution satellite remote sensing. J. Bridge Eng. 24 (12), 04019115.

Koseki, J. et al., 2018. Deformation evaluation by InSAR for efficient maintenance and management of road earth structures (in Japanese). Journal of JGS. 66 (10), 22–25.

Kubota, S., Ohta, S., Kimura, S., Pradeep, K., Tapas, D. K., 2024. Application example of interferometric SAR analysis to evaluate consolidation settlement behavior of river levees (in Japanese). Journal of JGS. 72 (1), 20–23.

Raspini, F., Cigna, F., Moretti, S., 2012. Multi-temporal mapping of land subsidence at basin scale exploiting Persistent Scatterer Interferometry: case study of Gioia Tauro plain (Italy). Journal of Maps, Vol. 8, No. 4, December, 514–524.

Rosen, P. A., Hensley, S., Joughin, I. R., Li, F. K., Madsen, S. N., Rodriguez, E., Goldstein, R. M., 2000. Synthetic aperture radar interferometry. Proc. IEEE. 88 (3), 333–382.

Rosi, A., Agostini, A., Tofani, V., Casagli. N., 2014. A Procedure to Map Subsidence at the Regional Scale Using the Persistent Scatterer Interferometry (PSI) Technique. Remote Sens. 6, 10510–10522.

Sadeghi, Z., Wright, T. J., Hooper, A. J., Jordan, C., Novellino, A., Bateson, L., Biggs, J., 2021. Benchmarking and inter-comparison of Sentinel-1 InSAR velocities and time series, Remote Sensing of Environment. 256, 112306.

Sato, H., Kondo, M., Kobori, T., Onodera, A., 2017. External deformation monitoring of nineteen rock fill dams using satellite SAR data (in Japanese). Civil Engineering Journal. 59–9, 36–41.

Solari, L., Ciampalini, A., Raspini, F., Bianchini, S., Moretti, S., 2016. PSInSAR analysis in the Pisa urban Area (Italy): a case study of subsidence related to stratigraphical factors and urbanization. Remote Sens. 8, 120.

Tanikawa, T., Hamada, J., Yamashita, K., 2025. Long-term settlement monitoring of a large building on soft ground using SAR satellite remote sensing (in Japanese). AIJ Journal of Technology and Design. Vol. 31, No.77, 169–174.

Wu, S., Yang, Z., Ding, X., Zhang, B., Zhang, L., Zhong, L., 2020. Two decades of settlement of Hong Kong International Airport measured with multi-temporal InSAR. Remote Sensing of Environment. 248, 111976.

Yamashita, K., Tanikawa, T., Uchida, A. 2019. Long-term behaviour of piled raft with DMW grid on reclaimed land, Geotechnical Engineering. Journal of the SEAGS & AGSSEA. 50 (3), 41–47.